

# Self-Attentive Adversarial Stain Normalization

Aman Shrivastava<sup>1\*</sup>, Will Adorno<sup>1\*</sup>, Lubaina Ehsan<sup>1</sup>,  
S. Asad Ali<sup>2</sup>, Sean R. Moore<sup>1</sup>, Beatrice C. Amadi<sup>3</sup>, Paul Kelly<sup>3,4</sup>,  
Donald E. Brown<sup>1†</sup>, Sana Syed<sup>1†</sup>

<sup>1</sup>University of Virginia, <sup>2</sup>Aga Khan University, Pakistan

<sup>3</sup>University of Zambia School of Medicine, Zambia

<sup>4</sup>Queen Mary University of London, United Kingdom  
{as3ek,wa3mr}@virginia.edu

## Abstract

Hematoxylin and Eosin (H&E) stained Whole Slide Images (WSIs) are utilized for biopsy visualization-based diagnostic and prognostic assessment of diseases. Variation in the H&E staining process across different lab sites can lead to significant variations in biopsy image appearance. These variations introduce an undesirable bias when the slides are examined by pathologists or used for training deep learning models. To reduce this bias, slides need to be translated to a common domain of stain appearance before analysis. We propose a Self-Attentive Adversarial Stain Normalization (SAASN) approach for the normalization of multiple stain appearances to a common domain. This unsupervised generative adversarial approach includes self-attention mechanism for synthesizing images with finer detail while preserving the structural consistency of the biopsy features during translation. SAASN demonstrates consistent and superior performance compared to other popular stain normalization techniques on H&E stained duodenal biopsy image data.

## Introduction

Histopathology involves staining patient biopsies for microscopic inspection to identify visual evidence of diseases. The most widely used stains in histopathology are Hematoxylin and Eosin (Fischer et al. 2008). Hematoxylin has a deep blue-purple color and stains acidic structures such as nucleic acids (DNA in cell nuclei). While Eosin is red-pink and stains basic structures such as nonspecific proteins in the cytoplasm and the stromal matrix. Staining, therefore, increases the visibility of the structural artifacts present in the biopsy, making it easier to examine. Further, these biopsies are digitized using slide scanning machines for future analysis and electronic transmission.

Computer vision is becoming increasingly useful in the field of histology for computed-aided diagnosis and discovering information about microscopic cell structures contained within histopathological images (Litjens et al. 2017). Digitized biopsies as high-dimensional datasets have proven to have tremendous potential in training deep learning algorithms for diagnosis and visual understanding of diseases.

Convolution Neural Networks (CNNs) have been applied for the prediction of the presence of disease using patches of whole slide images to diagnose breast cancer, enteropathies and other gastrointestinal diseases (Liu et al. 2017; Shrivastava et al. 2019; Wei et al. 2019). The performance and fairness of such data driven methods is dependent on the data that they are trained on. Therefore, it is of critical importance that the training data be free of any bias that might skew the models. A common source of such bias is significant variation in the stain color distribution from image to image. This is due to the discrepancies in the staining process that include tissue preparation, raw materials, manufacturing protocol, and digital scanners (Bejnordi et al. 2014) across different sites where these slides are prepared. Multiple H&E stain distributions within CNN input data can lead to biased predictions in which the results are influenced by color differences and not the cell structures of interest for clinical diagnostic interpretation. Additionally, it causes difficulty for a trained model to make predictions on a tissue with a new stain appearance that the model has not been trained on.

To overcome these issues, researchers have developed normalization techniques to convert all input images to an equivalent color distribution. Some of the most popular stain normalization techniques depend on a qualitatively chosen target image that represents an ideal color appearance (Maccenko et al. 2009; Khan et al. 2014; Vahadane et al. 2016). The input (source) image is normalized to match the stain profile of the chosen target image. The obvious downside to this approach is that the normalization is highly dependent on the color distribution of a single image. Rather than using just one target image to represent an entire stain distribution, an alternative approach is to consider an entire set of images that share the same stain distribution as the target domain. A mapping functions can then be learned to translate images from a particular source domain to the target domain. The problem can be modelled as an unsupervised image to image translation task (Liu, Breuel, and Kautz 2017).

Recently, Generative Adversarial Networks (GANs) have been shown to demonstrate exceptional results in unpaired image translation tasks (Yi et al. 2017; Zhu et al. 2017; Kim et al. 2017). The challenge posed by stain normaliza-

\*Equal contribution

†Co-corresponding author

tion task, however, is that during image translation it has to be made sure that the resulting image is as finely detailed as the input image, and also that the microscopic structural properties of the image are preserved in the process. Additionally, since the biopsy slides can be sourced from multiple sites, the framework should be capable of mapping different stain distributions to a common target distribution.

In this paper, we propose a novel adversarial approach that can execute *many-to-one* domain stain normalization. A custom loss function, structural cycle consistency loss, is designed to make sure that the structure of the image is preserved. Self-attention (Parikh et al. 2016) is used to ensure that highly detailed microscopic features can be synthesized in the image. Our approach and other leading stain normalization techniques are compared on duodenum biopsy image data that was used to diagnose Celiac or Environmental Enteropathy disease in children. SAASN demonstrated superior performance in preserving the structural integrity of images while transferring the stain distribution from one domain to the other.

## Related Work

The earliest methods that attempted stain normalization were primarily simple style transfer techniques. Histogram specification mapped the histogram statistics of the target image with the histogram statistics of the source (Coltuc, Bolon, and Chassery 2006). This approach only works well if the target and source images have similar color distributions. Forcing the normalization of the source image to match the histogram statistics of the target can create artifacts which alter the structural integrity. Color transfer with histogram specification can also be performed in a decorrelated CIELAB (LAB) color space (Reinhard et al. 2001). The LAB color space is designed to approximate the human visual system. For H&E stained histology images, the presence of each stain or the lack thereof at each pixel should represent the most appropriate color space. Considering this, researchers developed stain normalization methods that outperformed the histogram specification technique by leveraging stain separation.

These techniques start with converting RGB image into Optical Density ( $O_D$ ) as  $O_D = \log \frac{I_0}{I}$ , where  $I_0$  is the total possible illumination intensity of the image and  $I$  is the RGB image. Color Deconvolution (CD) is made easier in the OD space, because the stains now have a linear relationship with the OD values. The CD is typically expressed as  $O_D = VS$ , where  $V$  is the matrix of stain vectors and  $S$  is the stain density map. The stain density map can preserve the cell structures of the source image, while the stain vectors are updated to reflect the stain colors of the target image.

In Macenko et al. (Macenko), stain separation is computed using Singular Value Decomposition on the OD tuples. Planes are created from the two largest singular values to represent H&E stains. One useful assumption with this approach is that the color appearance matrix is non-negative which makes sense, because a stain value of zero would refer to the stain not being present at all. The approach by Vahadane et al. (Vahadane) also includes the non-

negative assumption as well as sparsity, which assumes that each pixel is characterized by an effective stain that relates to a particular cell structure (nuclei cells, cytoplasm, etc.). The stain separation is generated with Sparse Non-negative Matrix Factorization (SNMF) where the sparsity acts as a constraint to greatly reduce the solution space (Roy et al. 2018). SNMF is calculated using dictionary learning via the SPAMS package.

Macenko and Vahadane are both unsupervised techniques but there are also supervised approaches to this problem. Khan et al. applies a relevance vector machine or a random forest model to classify each pixel as hematoxylin, eosin or background. The authors provide a pre-trained model for cases where the stain color distribution of the source images is close to their training data. Training a new model would require a training set with pixel level annotations for each stain. After the stain separation, the color of the target image is mapped with a non-linear spline. The non-linear mapping approach can lead to undesirable artifacts and this normalization approach is more computationally costly than the unsupervised approaches.

Recently, techniques for stain normalization have progressed to include deep learning approaches such as autoencoders and GANs (Janowczyk, Basavanthally, and Madabhushi 2017; Shaban et al. 2019). The StainGAN approach (Shaban et al. 2019) applied the CycleGAN framework for *one-to-one* domain stain transfers. In a *one-to-one* stain transfer situation, the cycle-consistency loss is calculated by taking the  $L1$  distance between the cycled image and the ground truth. In a *many-to-one* situation, the cycled image will likely have a different color appearance than original image. Therefore, a new loss function that focuses on image structure and not the color differences is required.

Biopsy images contain a lot of repetitive patterns across the image in form of the recurring cell structures, stain gradients and background alike. While translation, these spatial dependencies can be used to synthesize realistic images with finer details. Self-attention (Parikh et al. 2016) exhibits impressive capability in modelling long range dependencies in images. SAGAN (Zhang et al. 2018) demonstrated the use of self-attention mechanism into convolutional GANs to synthesize images in a class conditional image generation task. We incorporate these advances in SAASN to enable it to efficiently find spatial dependencies in different areas of the image.

## Approach

The general objective of the proposed framework is to learn the mapping between stain distributions represented by domains  $X$  and  $Y$ . Since the aim of the approach is to make the stain patterns normalized over the entire dataset, one of these domains can be considered as the target domain (say  $Y$ ). The task is then to generate images that are indistinguishable from the images in the target domain based on stain differences. Stain normalization is a task that desires translation of images to a singular domain of stain distribution. This allows us to have multiple sub-domains in domain  $X$  representing different stain patterns. The overall objective then becomes to learn mapping functions  $G_{YX} : X \rightarrow Y$  and

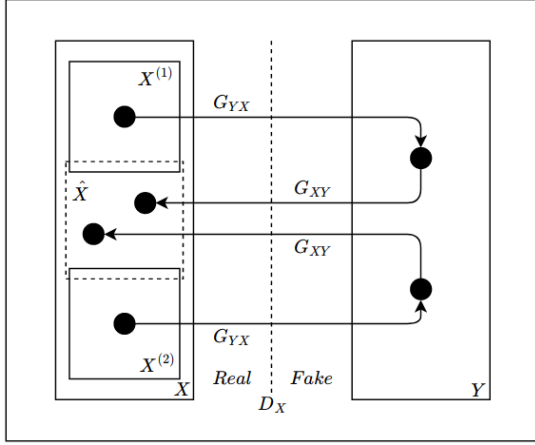


Figure 1: Visual example of a *many-to-one* stain transfer network. Two different stains are present as inputs within  $X$ :  $X^{(1)}$  and  $X^{(2)}$ . Both of these domains are translated to  $Y$  with  $G_{YX}$ . To complete the cycle,  $G_{XY}$  returns the image back to the  $X$  domain, but it can no longer be mapped directly to the input sub-domains  $X^{(1)}$  or  $X^{(2)}$  from which it originated. Instead, the image is mapped back to  $\hat{X}$  which represents a new domain of stain appearance.

$G_{XY} : Y \rightarrow X$  given unpaired training samples  $\{x_i^k\}_{i=1}^N$ ,  $x_i^k \in X^{(k)} \in X$ ,  $k \in [1, K]$  where  $K$  denotes the number of sub-domains in  $X$  and  $\{y_j\}_{j=1}^M$ ,  $y_j \in Y$ . The distribution of the training dataset is denoted as  $x \sim p(x | k)$  and  $y \sim p(y)$ . Additionally, two discriminator functions  $D_X$  and  $D_Y$  are used.  $D_X$  is employed to distinguish mapped images  $G_{XY}(y_i)$  from  $x_i$  while in a similar fashion  $D_Y$  is used to distinguish  $G_{YX}(x_i)$  from  $y_i$ . As illustrated in the Figure 1, the mapping function  $G_{XY}$  will map images from domain  $Y$  to a previously undefined sub-domain  $\hat{X}$  whose boundary is defined by the optimization function and the train data distributions in domain  $X$ . The overall optimization function used to train the designed framework includes a combination of *adversarial loss* (Goodfellow et al. 2014), *cycle consistency loss* (Zhu et al. 2017), *identity loss* (Taigman, Polyak, and Wolf 2016), *structural cycle consistency loss* based on the *structural similarity index* (Wang et al. 2004) and a *discriminator boundary control* factor.

**Adversarial loss** is used to ensure that the distribution of the generated images matches the distribution of the real (ground truth) images in that domain. The objective for the mapping function  $G_{YX} : X \rightarrow Y$  and the corresponding discriminator  $D_Y$  is defined as:

$$\mathcal{L}_{adv}^Y = \mathbb{E}_{y \sim p(y)} [\log D_Y(y)] + \mathbb{E}_{x \sim p(x|k)} [\log (1 - D_Y(G_{YX}(x)))] \quad (1)$$

Here  $G_{YX}$  tries to generate images that are indistinguishable from images in domain  $Y$  and consequently fool the discriminator  $D_Y$ , i.e. the generator  $G_{YX}$  tries to minimize the given objective function while the discriminator  $D_Y$  tries to

maximize it. Similarly the objective for the reverse mapping function  $G_{XY} : Y \rightarrow X$  is defined. The presence of multiple distinct stain distributions in the domain  $X$  can make it challenging for the discriminator  $D_X$  to learn the decision boundary surrounding the domain  $X$ . This can especially pose a challenge when there is an overlap or proximity in the stain distribution of one of the sub-domains of  $X$  and the target domain  $Y$  in the high-dimensional space. Therefore, to make sure that the decision boundary learned by  $D_X$  does not include sections of the target domain  $Y$ , a **discriminator boundary control** factor is added to the optimization function as follows:

$$\mathcal{L}_{adv}^X = \mathbb{E}_{x \sim p(x|k)} [\log D_X(x)] + \mathbb{E}_{y \sim p(y)} [\log (1 - D_X(G_{XY}(y)))] + \mathbb{E}_{y \sim p(y)} [\log (1 - D_X(y))] \quad (2)$$

**Cycle consistency loss** (Zhu et al. 2017) is implemented to reconcile with the unpaired nature of the task. To overcome the lack of a ground truth image for a fake image generated in a particular domain, the image is mapped back to its original domain using the reverse mapping function. The reconstructed image is then compared to the original source image to optimize the mapping function as follows:

$$\mathcal{L}_{cyc} = \mathbb{E}_{x \sim p(x|k)} [\|G_{XY}(G_{YX}(x)) - x\|_1] + \mathbb{E}_{y \sim p(y)} [\|G_{YX}(G_{XY}(y)) - y\|_1] \quad (3)$$

**Structural cycle consistency loss** is added to the objective function to alleviate the shortcomings of the cycle consistency loss for *many-to-one* translation. In a *many-to-one* situation the cycled images are likely to have a distinct color distribution than any of the sub-domains. Therefore minimizing the  $L1$  distance between original and the cycled image alone is not an effective way to ensure cycle consistency. We use a color agnostic structural dissimilarity loss based on the Structural Similarity (SSIM) index (Wang et al. 2004) as follows:

$$\mathcal{L}_{scyc} = \frac{1 - SSIM(G_{XY}(G_{YX}(x)), x)}{2} + \frac{1 - SSIM(G_{YX}(G_{XY}(y)), y)}{2} \quad (4)$$

Additionally, we need to make sure that the the mapping learnt by the generator does not result in the loss of biological artifacts in the images. The structural dissimilarity loss is also computed between the mapped and the original image:

$$\mathcal{L}_{dssim} = \frac{(1 - SSIM(G_{YX}(x), x))}{2} + \frac{(1 - SSIM(G_{XY}(y), y))}{2} \quad (5)$$

while

$$SSIM(a, b) = \frac{(2\mu_a\mu_b + C_1) + (2\sigma_{ab} + C_2)}{(\mu_a^2 + \mu_b^2 + C_1)(\sigma_a^2 + \sigma_b^2 + C_2)} \quad (6)$$

where  $\mu, \sigma$  are the respective means and standard deviations of the windows ( $a$  and  $b$ ) of the fixed size  $N \times N$  that strides over the input image.  $C_1$  and  $C_2$  are stabilizing factors that prevent the denominator from disappearing. These measures are calculated for multiple corresponding windows of gray-scaled input images and aggregated to get the final measure. Gray-scaled inputs are used to focus on structural differences between images and not changes in color.

**Identity loss** (Taigman, Polyak, and Wolf 2016) is utilized to regularize the generator and preserve the overall composition of the image. The generators are rewarded if a near identity mapping is produced when an image from the respective target domain is provided as an input image. In other words, when an image is fed into a generator of its own domain, the generator should produce an image that is nearly identical to the input. This is enforced by minimizing the  $L1$  distance of the resulting image with the input image as follows:

$$\mathcal{L}_{id} = \mathbb{E}_{y \sim p(y)} [\|G_{YX}(y) - y\|_1] + \mathbb{E}_{x \sim p(x|k)} [\|G_{XY}(x) - x\|_1] \quad (7)$$

The overall objective function then becomes:

$$\mathcal{L}(G_{YX}, G_{XY}, D_X, D_Y) = \mathcal{L}_{adv}^Y + \mathcal{L}_{adv}^X + \alpha * \mathcal{L}_{cyc} + \beta * \mathcal{L}_{scyc} + \gamma * \mathcal{L}_{dssim} + \delta * \mathcal{L}_{id} \quad (8)$$

where parameters  $\alpha, \beta, \gamma$  and  $\delta$  manage the importance of different loss terms. The parameters in the generators and the discriminators are tuned by solving the above objective as:

$$G_{YX}^*, G_{XY}^* = \arg \min_{G_{YX}, G_{XY}} \max_{D_X, D_Y} \mathcal{L}(G_{YX}, G_{XY}, D_X, D_Y) \quad (9)$$

In the following sections, we describe the implementation and compare our results with other current state-of-the-art methods of color normalization with both multiple ( $K = 2$ ) and single ( $K = 1$ ) sub-domains in  $X$ .

## Dataset and Implementation

### Dataset

For this paper, duodenal biopsy patches were extracted from 465 high resolution WSIs from 150 H&E stained duodenal biopsy slides (where each glass slide could have one or more biopsies). The biopsies were from patients with Celiac Disease (CD) and Environmental Enteropathy (EE). The biopsies were from children who underwent endoscopy procedures at either Aga Khan University Hospital in Pakistan (10 children <2 years with growth faltering, EE diagnosed on endoscopy,  $n = 34$  WSI), University Teaching Hospital in Zambia (16 children with severe acute malnutrition, EE diagnosed on endoscopy,  $n = 19$  WSI), or the University of Virginia Childrens Hospital (63 children <18 years old with CD,  $n = 236$  WSI; and 61 healthy children <5 years old,  $n = 173$  WSI). It was observed that there was a significantly large stain variation between images originating from different sites. While images from Pakistan were different

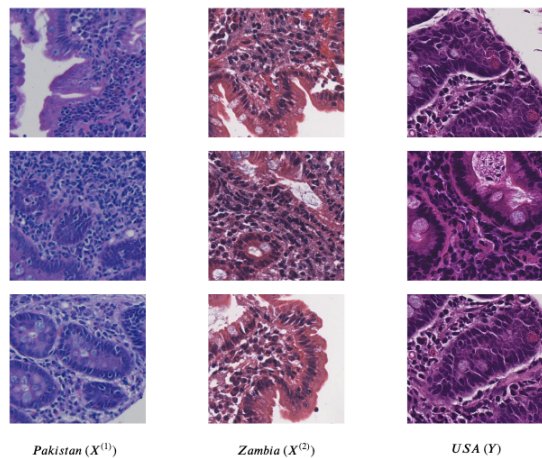


Figure 2: H&E stained duodenal biopsy patches created from whole slide images sourced from different locations.

tones of dark blue, images from USA were more pink with images from Zambia lying somewhere in the middle of this spectrum.

There is always some degree of physical variation between histological sections from different sites. In this study, our approach and other competing methods were performed on  $500 \times 500$  pixel patches generated from the images, which were further resized to  $256 \times 256$  pixel to marginally reduce the resolution. In the multi-sub-domain setup, patches from Pakistan (sub-domain  $X^{(1)}$ ) and Zambia (sub-domain  $X^{(2)}$ ) were both considered to be in domain  $X$  and patches from USA to be in domain  $Y$ . While in single sub-domain training setup, patches from Pakistan were considered to be in domain  $X$  and USA to be in domain  $Y$ . For training both  $X$  and  $Y$  had 11168 patches where  $X^{(1)}$  contributed 7817 and  $X^{(2)}$  3351 patches. Testing metrics were computed on 1500 patches in each sub-domain.

### Network Architecture

The generator network is a modified U-Net (Ronneberger, Fischer, and Brox 2015) which has been shown to generate excellent results in image translation tasks (Isola et al. 2017). U-Net is encoder-decoder network (Hinton and Salakhutdinov 2006) that uses skip connections between layers  $i$  and  $n - 1$  where  $n$  is the total number of layers in the network. In previous encoder-decoder architectures (Pathak et al. 2016; Wang and Gupta 2016; Yoo et al. 2016). The input is passed through a series of convolutional layers that downsample the input until a bottleneck is reached after which the information is upsampled to generate an output of the desired dimensions. Therefore, by design all information passes through the bottleneck. In a stain normalization task, the input and the output of the network share a lot of general information that might get obscured through the flow of such a network. Skip connections in a U-Net solve this problem by circumventing the bottleneck and concatenating the output from the encoder layers to the input of the corresponding decoder layers.

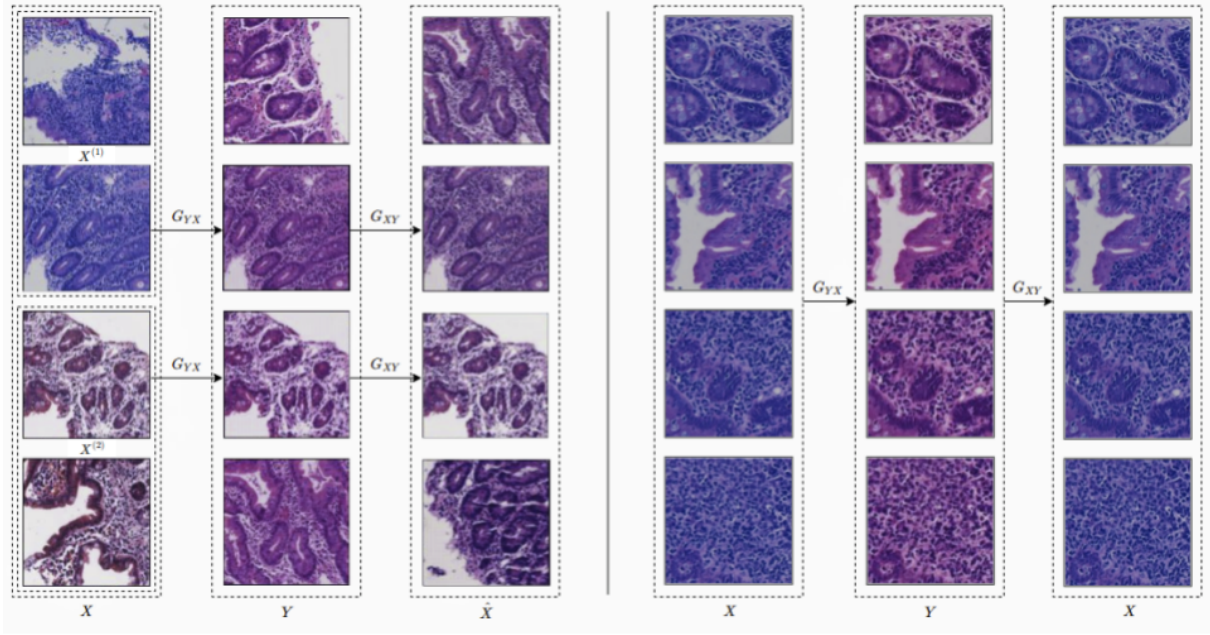


Figure 3: *Left*: Results when mapping was done from two sub-domains of  $X$  to  $Y$ . Patches from both domains  $X^{(1)}$  and  $X^{(2)}$  are translated to domain  $Y$  using  $G_{YX}$ . These generated images are then translated back to a new domain defined by a  $G_{XY}$  as a combination of stain distributions of sub-domains of  $X$ . Patches on either end of the second column are real images from domain  $Y$  and have been added to visually show the performance of  $G_{YX}$ . *Right*: Results when mapping was learnt using a single domain in  $X$  to  $Y$ .

The discriminator is a 4 block convolutional neural network, which eventually outputs the decision for each image. Every convolutional block in both the generator and the discriminator is a module consisting of a convolution-normalization-ReLU layers in that order. Both instance (Ulyanov, Vedaldi, and Lempitsky 2016) and batch (Ioffe and Szegedy 2015) normalization were used; and batch normalization was empirically chosen for the final network. The convolutional layers have kernel size of 4 and stride 2, with the exception of the last layer in the discriminator which operates with stride 1.

**Self-attention layers** (Parikh et al. 2016) were added after every convolutional block in both the generator and the discriminator network. The self-attention mechanism complements the convolutions by establishing and leveraging long range dependencies across image regions. It help the generator synthesize images with finer details in regions based on a different spatial region in the image. Additionally the discriminator with self-attention layers is able to enforce more complex structural constraints on input images while making a decision. As described in SAGAN (Zhang et al. 2018), a non-local network (Wang et al. 2018) was used to apply the self-attention computation. The input features  $x \in \mathbb{R}^{C \times N}$  are transformed using three different learnable functions  $q(x)$ ,  $k(x)$ ,  $v(x)$  analogous to query, key and value setup in (Vaswani et al. 2017) as follows:

$$q(x) = W_q x; \quad k(x) = W_k x; \quad v(x) = W_v x \quad (10)$$

where  $W_q \in \mathbb{R}^{\tilde{C} \times C}$ ,  $W_k \in \mathbb{R}^{\tilde{C} \times C}$ , and  $W_v \in \mathbb{R}^{\tilde{C} \times C}$ . Also,  $C$  is the number of channels,  $N = height * width$  of the feature map from the previous layer and  $\tilde{C}$  is an adjustable parameter. For our model,  $\tilde{C}$  was set as  $C/8$ . The attention map is further calculated as:

$$\begin{aligned} \alpha_{j,i} &= softmax(k(x_i)^T g(x_j)) \\ &= \frac{\exp(k(x_i)^T g(x_j))}{\sum_{i=1}^N \exp(k(x_i)^T g(x_j))} \end{aligned} \quad (11)$$

where  $\alpha_{j,i}$  represents the attention placed on location  $i$  while synthesizing location  $j$ . The output  $o \in \mathbb{R}^{C \times N}$  is calculated as:

$$o_j = \sum_{i=1}^N \alpha_{j,i} v(x_i) \quad (12)$$

The output  $o$  is then scaled and added to the initial input to give the final result,

$$y_i = \mu o_i + x_i \quad (13)$$

where  $\mu$  is a learnable parameter that is initialized to 0.

**Spectral normalization** when applied on the layers of the discriminator network has been shown to stabilize the training of a GAN (Miyato et al. 2018). Moreover, based on the findings about the effect of a generator's conditioning on its performance, Zhang et al. argue that while training a self-attention based GAN, both the generator and the discriminator can benefit from using spectral normalization. Therefore,

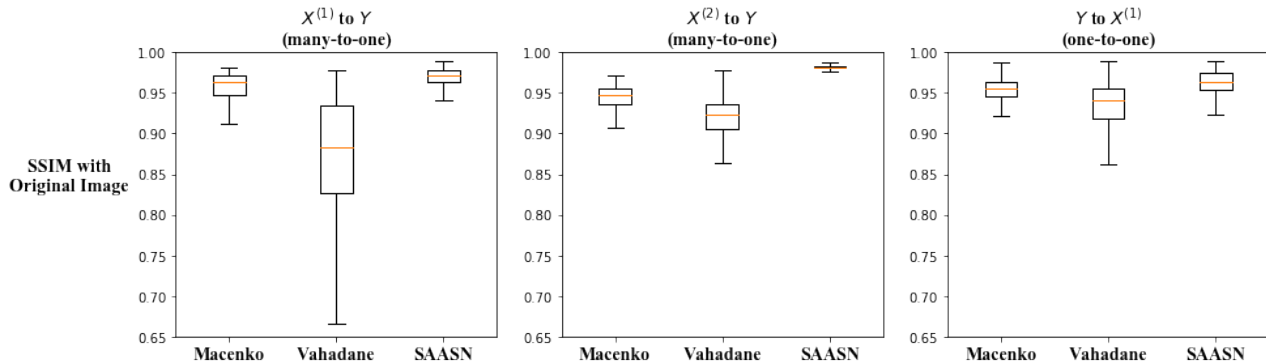


Figure 4: *Left:* Box plot for  $X^{(1)}$  to  $Y$  stain transfers. SAASN performed much better than Vahadane and slightly better than Macenko. *Center:* Box plot for  $X^{(2)}$  to  $Y$  stain transfers. SAASN performed much better than the other two methods and with much lower variance. *Right:* Box plot for  $Y$  to  $X^{(1)}$  stain transfers. Methods have similar performance, but SAASN does slightly better than Macenko.

a spectral normalization (with spectral norm of all weight layers as 1) was added to all the networks.

### Training Details

The parameter values of  $\alpha = 10$ ,  $\beta = 2$ ,  $\gamma = 1$  and  $\delta = 5$  were empirically chosen after experimentation for the evaluation model. Across all experiments, we used the Adam optimizer (Kingma and Ba 2014) with a learning rate of 0.0002. The model was trained for the first 50 epochs with a fixed learning rate and the next 50 epochs while linearly decaying the learning rate to 0. Instead of updating the discriminator with an image generated from the latest generator, a random image selected from a buffer of 50 previously generated images was used to perform the update cycle (Shrivastava et al. 2017). Least-squares adversarial loss inspired from LS-GAN (Mao et al. 2017) was used instead of the described cross-entropy loss for some experiments. The least-squares loss stabilized the training but there was no significant visual difference in the results produced.

### Results and Evaluation

The SAASN approach is compared to two of the most popular unsupervised stain normalization techniques, Macenko (Macenko et al. 2009) and Vahadane (Vahadane et al. 2016). The popular supervised approach by Khan (Khan et al. 2014) could not be tested, because the default pre-trained classifier performed poorly when transferring stains for these stain domains. We did not have access to data with stain labels per pixel to use for us to train our own classifier for this method. Two different SAASN networks are tested: the *many-to-one* and a *one-to-one* stain transfer approaches. The *many-to-one* network demonstrates that the SAASN approach can transfer multiple stain domains to a single domain. The  $X^{(1)}$  to  $Y$  and  $X^{(2)}$  to  $Y$  stain transfers are evaluated from this network. The *one-to-one* network is utilized to evaluate the  $Y$  to  $X^{(1)}$  stain transfer.

To evaluate the stain transfer, the Structural Similarity (SSIM) index is again utilized. SSIM is calculated by com-

paring the normalized image with the original. Both images are converted to gray-scale before beginning SSIM calculations. For color images, SSIM is influenced greatly by the differences in color for each image. A change in color is expected when performing stain transfers, so SSIM on RGB images is not an effective measure in this case. The main concern is whether the structural integrity of the image is maintained after transferring stains which is why gray-scaled images are used. Additionally, visual comparisons are provided to evaluate stain transfer capability.

SSIM scores were calculated on test sets for each of the three stain normalization techniques. The results are compiled and displayed as box plots in Figure 4. For the  $X^{(1)}$  to  $Y$  and the  $X^{(2)}$  to  $Y$  stain transfers, the median values for SAASN are higher than the other two normalizations and the interquartile ranges are much smaller. This demonstrates that SAASN not only is better at preserving structure, but also consistently transfers stain without many anomalies. The unsupervised approaches can struggle if the source has a much different stain distribution than the target. This can lead to the stains appearing in the wrong areas on the normalized image. SAASN is able to leverage information from entire stain domains and therefore is not as affected by this issue. Patches with erroneous stain transfers can hinder the development of computer-aided diagnosis models. These results demonstrate that SAASN can be trusted to produce consistent stain transfers on a robust set of stain patterns in WSI patches.

In addition to assessing the structure-preserving ability of the stain normalization methods, visual comparisons are useful to ensure that the stains have transferred properly. In Figure 5, results are displayed for the three stain transfers. The images with the smallest  $L_2$ -norm for combined Macenko and Vahadane SSIM values were selected to demonstrate the performance of SAASN. For  $X^{(1)}$  to  $Y$  and  $X^{(2)}$  to  $Y$ , the same target image from domain  $Y$  is used. For  $Y$  to  $X^{(1)}$ , a target image from domain  $X^{(1)}$  is used. The three selected source images are similar in that they all have a large majority of pixels containing connective tissue or back-

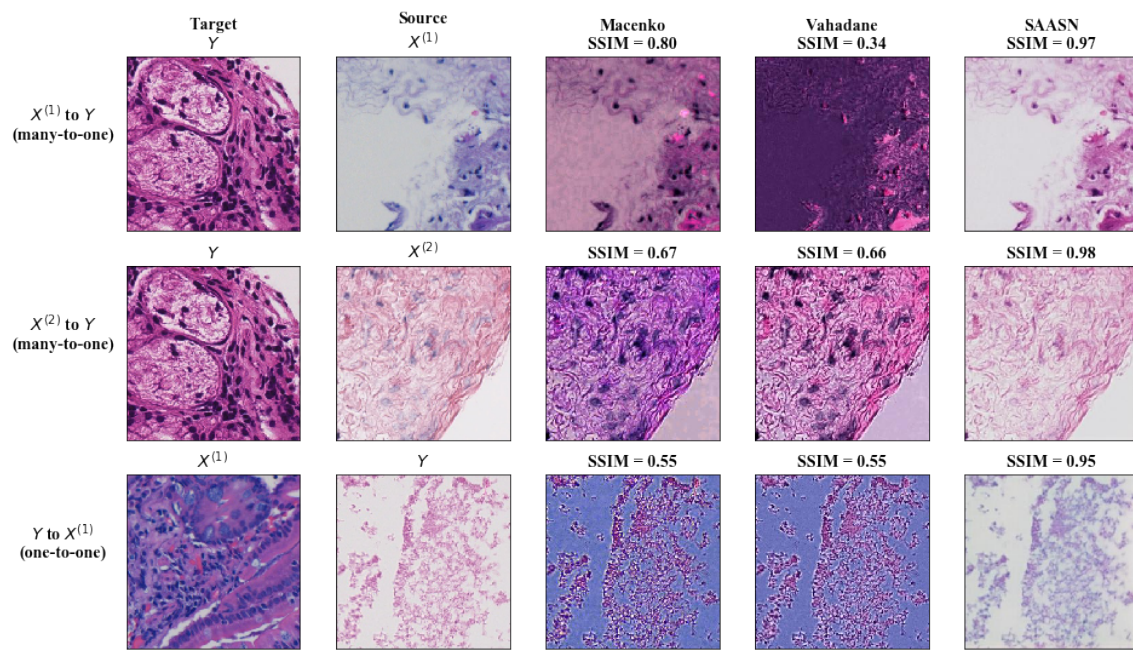


Figure 5: Visual comparison of performance in cases where Macenko and Vahadane struggle at transferring the right stain to the right location. The target image only applies to the Macenko and Vahadane techniques.

ground. The unsupervised approaches can struggle executing color deconvolution on these types of images. This is apparent in the Macenko and Vahadane normalizations shown in Figure 5. The stains are either inverted (hematoxylin-like color transferred to the background) or confusing connective tissue as an actual cell structure. Meanwhile, SAASN did not have difficulty identifying the connective tissue or background pixels in the source image. SAASN excelled at preserving structural similarity with the source image and successfully transferred the stain to a new domain without error. Trained model, code and extra results have been made publicly available<sup>1</sup>.

## Conclusions

The proposed framework was successful in effective translation of images from one stain appearance to a desired one while preserving the biological artifacts in the process. This setup was specifically designed to accommodate a *many-to-one* stain transfer situation in which multiple stains are converted to a common domain. SAASN is compared to other leading stain normalization techniques using duodenal biopsy image data originating from three sites with different stain variations. Results showed that SAASN performed the best at preserving the structure of the source image after the stain transfer. SAASN consistently performed successful stain transfers even when the other techniques failed due to large variations between the source and target image stains and unconventional input image structures. We contend that the proposed unsupervised image to image translation can

be successfully applied to general *many-to-one* image translation problems outside the medical domain as well.

## Acknowledgements

Research reported in this publication was supported by the University of Virginia Translational Health Research Institute of Virginia (THRIV) Mentored Career Development Award (SS), the Bill and Melinda Gates Foundation (AA, OPP1138727; SRM, OPP1144149; PK, OPP1066118) and by the National Institute Of Diabetes And Digestive And Kidney Diseases of the National Institutes of Health under Award Number K23DK117061. The content is solely the responsibility of the authors and does not necessarily represent the official views of the National Institutes of Health.

## References

- [Bejnordi et al. 2014] Bejnordi, B. E.; Timofeeva, N.; Otte-Höller, I.; Karssemeijer, N.; and van der Laak, J. A. 2014. Quantitative analysis of stain variability in histology slides and an algorithm for standardization. In *Medical Imaging 2014: Digital Pathology*, volume 9041, 904108. International Society for Optics and Photonics.
- [Coltuc, Bolon, and Chassery 2006] Coltuc, D.; Bolon, P.; and Chassery, J.-M. 2006. Exact histogram specification. *IEEE Transactions on Image Processing* 15(5):1143–1152.
- [Fischer et al. 2008] Fischer, A. H.; Jacobson, K. A.; Rose, J.; and Zeller, R. 2008. Hematoxylin and eosin staining of tissue and cell sections. *Cold Spring Harbor Protocols* 2008(5):pdb-prot4986.
- [Goodfellow et al. 2014] Goodfellow, I.; Pouget-Abadie, J.; Mirza, M.; Xu, B.; Warde-Farley, D.; Ozair, S.; Courville, A.; and Bengio, Y. 2014. Generative adversarial nets. In *Advances in neural information processing systems*, 2672–2680.

<sup>1</sup>Redacted for blind review

- [Hinton and Salakhutdinov 2006] Hinton, G. E., and Salakhutdinov, R. R. 2006. Reducing the dimensionality of data with neural networks. *science* 313(5786):504–507.
- [Ioffe and Szegedy 2015] Ioffe, S., and Szegedy, C. 2015. Batch normalization: Accelerating deep network training by reducing internal covariate shift. *arXiv preprint arXiv:1502.03167*.
- [Isola et al. 2017] Isola, P.; Zhu, J.-Y.; Zhou, T.; and Efros, A. A. 2017. Image-to-image translation with conditional adversarial networks. In *Proceedings of the IEEE conference on computer vision and pattern recognition*, 1125–1134.
- [Janowczyk, Basavanthally, and Madabhushi 2017] Janowczyk, A.; Basavanthally, A.; and Madabhushi, A. 2017. Stain normalization using sparse autoencoders (stanosa): Application to digital pathology. *Computerized Medical Imaging and Graphics* 57:50–61.
- [Khan et al. 2014] Khan, A. M.; Rajpoot, N.; Treanor, D.; and Magee, D. 2014. A nonlinear mapping approach to stain normalization in digital histopathology images using image-specific color deconvolution. *IEEE Transactions on Biomedical Engineering* 61(6):1729–1738.
- [Kim et al. 2017] Kim, T.; Cha, M.; Kim, H.; Lee, J. K.; and Kim, J. 2017. Learning to discover cross-domain relations with generative adversarial networks. In *Proceedings of the 34th International Conference on Machine Learning-Volume 70*, 1857–1865. JMLR.org.
- [Kingma and Ba 2014] Kingma, D. P., and Ba, J. 2014. Adam: A method for stochastic optimization. *arXiv preprint arXiv:1412.6980*.
- [Litjens et al. 2017] Litjens, G.; Kooi, T.; Bejnordi, B. E.; Setio, A. A. A.; Ciompi, F.; Ghafoorian, M.; Van Der Laak, J. A.; Van Ginneken, B.; and Sánchez, C. I. 2017. A survey on deep learning in medical image analysis. *Medical image analysis* 42:60–88.
- [Liu et al. 2017] Liu, Y.; Gadepalli, K. K.; Norouzi, M.; Dahl, G.; Kohlberger, T.; Venugopalan, S.; Boyko, A. S.; Timofeev, A.; Nelson, P. Q.; Corrado, G.; Hipp, J.; Peng, L.; and Stumpe, M. 2017. Detecting cancer metastases on gigapixel pathology images. Technical report, arXiv.
- [Liu, Breuel, and Kautz 2017] Liu, M.-Y.; Breuel, T.; and Kautz, J. 2017. Unsupervised image-to-image translation networks. In *Advances in neural information processing systems*, 700–708.
- [Macenko et al. 2009] Macenko, M.; Niethammer, M.; Marron, J. S.; Borland, D.; Woosley, J. T.; Guan, X.; Schmitt, C.; and Thomas, N. E. 2009. A method for normalizing histology slides for quantitative analysis. In *2009 IEEE International Symposium on Biomedical Imaging: From Nano to Macro*, 1107–1110. IEEE.
- [Mao et al. 2017] Mao, X.; Li, Q.; Xie, H.; Lau, R. Y.; Wang, Z.; and Paul Smolley, S. 2017. Least squares generative adversarial networks. In *Proceedings of the IEEE International Conference on Computer Vision*, 2794–2802.
- [Miyato et al. 2018] Miyato, T.; Kataoka, T.; Koyama, M.; and Yoshida, Y. 2018. Spectral normalization for generative adversarial networks. *arXiv preprint arXiv:1802.05957*.
- [Parikh et al. 2016] Parikh, A. P.; Täckström, O.; Das, D.; and Uszkoreit, J. 2016. A decomposable attention model for natural language inference. *arXiv preprint arXiv:1606.01933*.
- [Pathak et al. 2016] Pathak, D.; Krahenbuhl, P.; Donahue, J.; Darrell, T.; and Efros, A. A. 2016. Context encoders: Feature learning by inpainting. In *Proceedings of the IEEE conference on computer vision and pattern recognition*, 2536–2544.
- [Reinhard et al. 2001] Reinhard, E.; Adhikhmin, M.; Gooch, B.; and Shirley, P. 2001. Color transfer between images. *IEEE Computer graphics and applications* 21(5):34–41.
- [Ronneberger, Fischer, and Brox 2015] Ronneberger, O.; Fischer, P.; and Brox, T. 2015. U-net: Convolutional networks for biomedical image segmentation. In *International Conference on Medical image computing and computer-assisted intervention*, 234–241. Springer.
- [Roy et al. 2018] Roy, S.; kumar Jain, A.; Lal, S.; and Kini, J. 2018. A study about color normalization methods for histopathology images. *Micron* 114:42–61.
- [Shaban et al. 2019] Shaban, M. T.; Baur, C.; Navab, N.; and Albarqouni, S. 2019. Staingan: Stain style transfer for digital histological images. In *2019 IEEE 16th International Symposium on Biomedical Imaging (ISBI 2019)*, 953–956. IEEE.
- [Shrivastava et al. 2017] Shrivastava, A.; Pfister, T.; Tuzel, O.; Susskind, J.; Wang, W.; and Webb, R. 2017. Learning from simulated and unsupervised images through adversarial training. In *Proceedings of the IEEE conference on computer vision and pattern recognition*, 2107–2116.
- [Shrivastava et al. 2019] Shrivastava, A.; Kant, K.; Sengupta, S.; Kang, S.-J.; Khan, M.; Ali, A.; Moore, S. R.; Amadi, B. C.; Kelly, P.; Brown, D. E.; et al. 2019. Deep learning for visual recognition of environmental enteropathy and celiac disease. *arXiv preprint arXiv:1908.03272*.
- [Taigman, Polyak, and Wolf 2016] Taigman, Y.; Polyak, A.; and Wolf, L. 2016. Unsupervised cross-domain image generation. *arXiv preprint arXiv:1611.02200*.
- [Ulyanov, Vedaldi, and Lempitsky 2016] Ulyanov, D.; Vedaldi, A.; and Lempitsky, V. 2016. Instance normalization: The missing ingredient for fast stylization. *arXiv preprint arXiv:1607.08022*.
- [Vahadane et al. 2016] Vahadane, A.; Peng, T.; Sethi, A.; Albarqouni, S.; Wang, L.; Baust, M.; Steiger, K.; Schlitter, A. M.; Esposito, I.; and Navab, N. 2016. Structure-preserving color normalization and sparse stain separation for histological images. *IEEE transactions on medical imaging* 35(8):1962–1971.
- [Vaswani et al. 2017] Vaswani, A.; Shazeer, N.; Parmar, N.; Uszkoreit, J.; Jones, L.; Gomez, A. N.; Kaiser, Ł.; and Polosukhin, I. 2017. Attention is all you need. In *Advances in neural information processing systems*, 5998–6008.
- [Wang and Gupta 2016] Wang, X., and Gupta, A. 2016. Generative image modeling using style and structure adversarial networks. In *European Conference on Computer Vision*, 318–335. Springer.
- [Wang et al. 2004] Wang, Z.; Bovik, A. C.; Sheikh, H. R.; Simoncelli, E. P.; et al. 2004. Image quality assessment: from error visibility to structural similarity. *IEEE transactions on image processing* 13(4):600–612.
- [Wang et al. 2018] Wang, X.; Girshick, R.; Gupta, A.; and He, K. 2018. Non-local neural networks. In *Proceedings of the IEEE Conference on Computer Vision and Pattern Recognition*, 7794–7803.
- [Wei et al. 2019] Wei, J. W.; Wei, J. W.; Jackson, C. R.; Ren, B.; Suriawinata, A. A.; and Hassanpour, S. 2019. Automated detection of celiac disease on duodenal biopsy slides: A deep learning approach. *Journal of pathology informatics* 10.
- [Yi et al. 2017] Yi, Z.; Zhang, H.; Tan, P.; and Gong, M. 2017. Dualgan: Unsupervised dual learning for image-to-image translation. In *Proceedings of the IEEE international conference on computer vision*, 2849–2857.
- [Yoo et al. 2016] Yoo, D.; Kim, N.; Park, S.; Paek, A. S.; and Kweon, I. S. 2016. Pixel-level domain transfer. In *European Conference on Computer Vision*, 517–532. Springer.
- [Zhang et al. 2018] Zhang, H.; Goodfellow, I.; Metaxas, D.; and



Odena, A. 2018. Self-attention generative adversarial networks. *arXiv preprint arXiv:1805.08318*.

[Zhu et al. 2017] Zhu, J.-Y.; Park, T.; Isola, P.; and Efros, A. A. 2017. Unpaired image-to-image translation using cycle-consistent adversarial networks. In *Proceedings of the IEEE international conference on computer vision*, 2223–2232.